Coherent Nanointerfaces in Thermoelectric Materials

Xiaopeng Huang and Xinwei Wang*

2010 Black Engineering Building, Department of Mechanical Engineering, Iowa State University, Ames, Iowa 50011, United States

Bruce Cook

221 Metals Development, Division of Materials Science & Engineering, Ames Laboratory, Iowa State University, Ames, Iowa 50011, United States

In recent years, a new type of bulk nanostructured thermoelectric material $Ag_{1-x}Pb_mSbTe_{2+m}$ (LAST) has been developed featuring significantly improved figure of merit (*ZT*) (up to 2.1 at 800 K). Its excellent *ZT* is largely attributed to the nanoscale coherent interface that promotes phonon scattering while having minimal effect on electron transport. Despite the experimental work on LAST material synthesis and characterization, very little knowledge is known about the nanoscale coherent interface and its effect on energy transport. In this work, we report on the first atomic observation of coherent nanointerface in a PbTe/GeTe nanocomposite and quantitative characterization of the local chemical composition and crystalline structure based on atomistic modeling. The structure coherency is confirmed with atom position imaging, atom number density distribution, and line and point coherency functions. Lattice matching occurs at the interface with lattice twisting and extremely localized strain ($\epsilon \approx 0.007$) in a region of 5−6 nm in GeTe. The localized strain field also helps reduce the thermal transport in the material. The effective lattice thermal conductivity of the nanocomposite at 700 K is calculated at 1.23 W m^{-1} K^{-1}, which is lower than that of many common thermoelectric materials. The low interfacial thermal resistance $7.3 \pm 0.3 \times 10^{-10}$ m^2 K W^{-1} illustrates weak interface phonon scattering by the coherent interface structure. This coherent interface is credited with very little electrical conductivity reduction, which is crucial for design of high *ZT* thermoelectric materials.

1. Introduction

In recent years, the increasing global energy demand has focused attention on renewable energy sources including wind energy, biofuels, fuel cells, and thermoelectric energy. Considerable research has been conducted to seek high efficiency thermoelectric (TE) materials. Examples of such efforts can be evidenced in several reviews on TE materials.[1−3] The performance of TE materials and devices is determined by the figure of merit $ZT = S^2\sigma T/k$, where *S* is the thermopower or Seebeck coefficient, σ is the electrical conductivity, *k* ($k_{lat} + k_e$) is the thermal conductivity, which is comprised of the lattice (k_{lat}) and electronic (k_e) components, and *T* is the absolute temperature. Significant effort has been focused on increasing *ZT* by reducing the lattice thermal conductivity k_{lat} through introduction of soluble second phases,[1] mass fluctuation alloying,[2] or nanostructures such as superlattices,[3,4] quantum dots,[3,4] embedded nanostructures,[5,6] and nanowires.[7] While phonon scattering is significantly enhanced by these structures, the electron scattering is also enhanced, leading to a reduction in electrical conductivity. The direct consequence is limited *ZT* improvement for TE materials.

Recently, a novel-type bulk TE material, coherent nanostructured TE material, has been proposed and synthesized to show great potential to significantly reduce k_{lat} while minimally altering the electrical conductivity. In the pioneering work by Hsu et al.,[8] coherent nanostructured bulk thermoelectric materials $AgPb_mSbTe_{2+m}$ with $m = 10$ and 18 were synthesized. *ZT* values

as high as 2.1 were reported at 800 K. Coherent interfaces were observed at the inclusion−matrix interface. The nanoscale inclusions were rich in Ag−Sb, while the matrix was deficient in Ag−Sb. The authors attributed the enhanced thermoelectric properties to the Ag−Sb enriched nanodots in the matrix. Subsequently, the same group[9] reported on the nature of thermoelectric materials $Ag_{1-x}Pb_mSbTe_{m+2}$ or LAST-*m* materials (LAST for lead antimony silver tellurium) with different *m* values. In their work[10] on $Ag_{0.85}SnSb_{1.15}Te_3$, they clearly indicated that the nanoinclusions are coherently embedded in the matrix and do not disrupt the surrounding atomic order, leading to minimal electron scattering. They suggested that the nanostructures efficiently scatter phonons in the materials, which leads to the very low thermal conductivity, as observed in their measurement. In the work by Zhou et al.[11] on nanostructured AgPbSbTe bulk materials, Ag−Sb-rich nanostructures were also observed, along with coherent interfaces. They pointed out that such coherent nanoclusions will result in a negligible disturbance to the electronic flow. A *ZT* value as large as 1.4 for $Ag_nPb_{18+x}SbTe_{20}$ bulk materials with a coherent interface structure at temperatures close to 700 K was also reported by Wang et al.[12]

The unambiguous presence of coherent interfaces was also observed in PbTe prepared with 4% Sb, 4% Bi, and 4% InSb by Hogan et al.[13] In a recent work by Cook et al.,[14] a detailed structural study of LAST-*m* was reported. Coherent interfaces were observed between the matrix and nanoscale inclusions, accompanied by a significant lattice strain at the interface. This type of coherent nanointerface offers three advantages in thermal

* To whom correspondence should be addressed. E-mail: xwang3@iastate.edu. Phone: 515-294-2085. Fax: 515-294-3261.
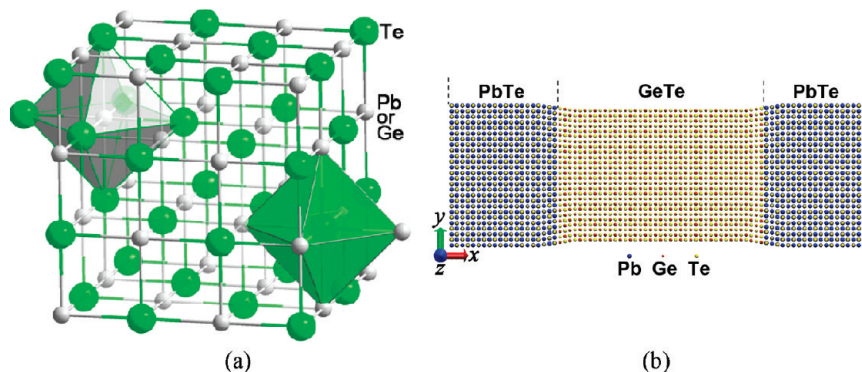
Figure 1. Structure of the modeling system. (a) NaCl-type crystal structure of PbTe and GeTe. (b) The initial PbTe/GeTe nanocomposite with gradient coherent interface.

design for *ZT* improvement: (1) the nanoscale inclusions significantly reduce the mean free path of phonons, thereby reducing k_{lat}; (2) the strain at the coherent interface significantly enhances phonon scattering and gives rise to a large interfacial thermal resistance, which helps reduce the overall *k* further; (3) the coherent interfacial structure produces very little electron scattering, resulting in a minimal decrease to the electrical conductivity. Such effect is very favorable for *ZT* improvement.

A significant amount of prior research has been conducted on other aspects of PbTe- or GeTe-based TE materials. Examples include the work on the mechanically stable PbTe,[15] PbTe nanocrystalline composites,[16] PbTe nanowires,[17,18] PbTe nanotubes,[19] PbTe quantum dot superlattice,[3] and amorphous/nanocrystalline hybrid GeTe.[20] It has been shown that doping p-type PbTe with thallium results in a perturbation in the electronic density of states which nearly doubles the materials' *ZT*.[21] Furthermore, considerable studies of PbTe- or GeTe-based composite materials have been performed, including PbTe-Ge and PbTe-Ge$_{1-x}$Si$_x$,[22] (PbTe)$_{1-x}$/(PbSe)$_x$,[23] PbTe nanocomposites,[24] and PbTe−Pb−Sb nanostructures.[5] In a recent work by Ikeda et al.,[25] self-assembled nanometer lamellae of PbTe-Sb$_2$Te$_3$ were synthesized, and epitaxy-like interfaces were observed. Such epitaxy-like interfaces are similar to the coherent interface discussed above.

Regarding the aforementioned coherent nanostructured TE materials, although the researchers realized that the coherent nanostructures play a critical role in enhancing phonon scattering and reducing thermal conductivity while having little effect on the electrical conductivity, the physics of thermal conductivity reduction is far from clear. Additionally, it remains unclear how and to what extent the coherent nanostructures reduce the thermal conductivity. The coherent nanostructures are far from optimized in terms of thermal conductivity reduction and *ZT* enhancement.

In this work, a molecular dynamics (MD) technique is used to explore the structure of a model coherent nanointerface, the strain in the lattice structure, and the local phonon energy transport mechanism. The PbTe/GeTe interface is selected for this work. This represents the first atomic understanding of the local coherent interface structure and the science of phonon scattering and thermal conductivity in coherent nanostructured materials.

2. Methodology

As one of the foremost computational methods in science, MD simulation provides details of 3D nanostructure and an understanding of the mechanisms responsible for thermal transport, mechanics, and even chemical reaction in materials,

which are nearly intractable from current experimental technology. This technique has already been applied to heat-transfer problems for some time. It was reviewed in detail by Chou et al.[26] and Chen et al.[27] As for research on thermal transport near interfaces, MD simulations have only been attempted in recent years. Since Maiti et al.[28] used nonequilibrium molecular dynamics (NEMD) in 1997 to study the Kapitza resistance across grain boundary, investigations on the interfaces between liquid and solid,[29] solid and solid,[30] and nanotube and nanotube[31] have been carried out. Since that time, the thermal conductivity of a number of thermoelectric materials, such as Bi$_2$Te$_3$,[32] Pb$_{1-x}$Sn$_x$Te and Pb$_{1-x}$Ge$_x$Te,[33] nanoporous Si,[34] Si/Ge nanocomposites,[35] and Si/Si$_{1-x}$Ge$_x$ superlattices[36] has also been investigated using MD. However, coherent nanostructured (PbTe)$_x$(GeTe)$_{1-x}$, as a promising candidate of excellent TE material, has not yet been examined. In the following sections, we will describe the application of MD to the investigation of this structure and the study of thermal transport within it.

2.1. Initial Structure Configuration and the Atomic Potential. As self-doping, narrow gap semiconductors, PbTe and GeTe have been widely studied for infrared detector devices in addition to thermoelectric applications. PbTe has a stable face-centered cubic (FCC) structure of NaCl type, and GeTe is characterized by a distortion from the cubic NaCl structure along the [111] direction with a sublattice shift at room temperature, which becomes the rhombohedral phase. However, above a critical temperature T_c, this material experiences a second-order phase transition to the NaCl type structure. The transition temperature T_c was found to be dependent on the Ge to Te ratio, 733 and 663 K for Ge-rich and Te-rich GeTe, respectively.[37] Ab initio calculation also predicted that for pure GeTe, $T_c = 657 \pm 100$ K.[38] In consideration of the accuracy of previous experiments and calculations, it is common knowledge that for pure GeTe the structure is rhombohedral below 700 K and NaCl-like above 700 K. Thus, for the convenience of structure modeling, an equilibrium temperature of 700 K is chosen for the MD simulation, at which PbTe and GeTe are both initialized with a cubic NaCl type structure, shown in Figure 1a.

PbTe and GeTe have lattice constants of $a_{PbTe} = 6.462$ Å and $a_{GeTe} = 5.987$ Å,[39] respectively. With different lattice constants, it is of interest to determine the structure of the interface between these phases when they are synthesized together in a matrix-nanoinclusion arrangement. Models such as acoustic mismatch model (AMM) and diffuse mismatch model (DMM) are the dominant theories developed in recent years.[40−43] As research has progressed, coherent interfaces have been observed in numerous composites by many groups, as described in the previous section. A coherent interface means

Coherent Nanointerfaces

J. Phys. Chem. C, Vol. 114, No. 49, 2010 **21005**

that the lattice planes of two materials at the interface become strained in order to produce a one-to-one matching at the boundary, while preserving each composition's distinct structure. This is opposed to formation of a distinct, strain-free boundary in the case of an incoherent interface, in which the lattice planes exhibit no regularity of matching. The acoustic mismatch still exists which can cause phonon scattering. An initial PbTe/GeTe coherent interface is constructed as shown in Figure 1b at the beginning of the MD modeling. Such an interface will self-adjust/relax to reach its natural stable structure, coherent or not. In the figure, the center corresponds to GeTe, bounded by PbTe at both ends. Both phases have the same number of atoms in the y-z layers. The difference is PbTe has a larger lattice constant than GeTe. For the initial structure, 3 y-z layers of PbTe and 3 y-z layers of GeTe adjacent to their interface are constructed to make the atomic distances in the y and z directions gradually change from a_{PbTe} to a_{GeTe}. In the x direction, PbTe and GeTe in these layers have the same atomic distance, which is the average value of the two lattice constants.

In this work, the Coulomb ionic potential combined with a modified Morse potential are used to describe the interaction between dynamic Pb^{2+}, Ge^{2+} and Te^{2-} ions as proposed by Chonan.[33] For ions i and j, the potential function is represented by

$$u_{ij}(r) = \frac{Cq_i q_j}{\varepsilon r} + f_0(b_i + b_j) \exp\left[\frac{a_i + a_j - r}{b_i + b_j}\right] \quad (1)$$

where r is the distance between ions, C is an energy-conversion constant, q_i and q_j are the charges on the 2 atoms, ε is the dielectric constant, and a_i and b_i are the effective radius and softness parameter of the ith ion with the standard force f_0, respectively. The values of these parameters are detailed in another work.[33]

2.2. MD Basics and Thermal Properties Calculation. In this work, NEMD is employed to calculate the thermal properties within the principle of phonon scattering events and local thermal equilibrium. Periodic boundary conditions in the three dimensions are used to simulate composites. The thermal conductivity k is governed by the Fourier's law $J = -k\nabla T$, where J is the heat flux and ∇T is the temperature gradient along the heat flow direction. There are two ways to obtain k. One is calculating the heat flux while maintaining the two ends at different constant temperatures. The other approach involves obtaining the temperature gradient when a given heat flux is known. As suggested by Huang,[35] the second approach is chosen in this work to minimize computational time. To apply a heat flux in one direction with periodic boundary conditions in NEMD, the algorithm developed by Ikeshoji and Hafskjold[44] is used. In this method, a fixed amount of energy in a given time period is added to a hot slab by scaling each hot atom's thermal movement by the same factor while momentum is conserved. A similar procedure is performed to a cold slab to remove the same amount of energy over the same time interval. For the structure in this work, the hot slab consists of four atomic layers in the center of the GeTe portion, and the cold slabs are two atomic layers at each PbTe end along the x direction. When the system reaches steady state, a temperature gradient will be established along the heat flux direction. To obtain the temperature gradient, the structure is divided into several sections along the x direction for statistical sampling of temperatures. Each section contains 2 atomic layers which have sufficient numbers of atoms to satisfy the principle of phonon scattering events.

The temperature of each section is calculated from the time-averaged kinetic energy within the simulation time using the energy equipartition theorem.[35] No quantum correction for the temperature is needed. This is because the Debye temperatures of PbTe and GeTe are 160[45] and 166 K,[46] respectively, which are much lower than the equilibrium temperature 700 K used in this work. When the temperature profile is obtained, the interfacial thermal resistance could also be calculated by $R''_{tc} = \Delta T/J$ except for getting the thermal conductivity of the system, where ΔT is the temperature drop across the interface. The temperature drop across the interface will be obtained by linear fitting of the temperature at two sides of the interface as detailed later.

2.3. Simulation Conditions. As shown in Figure 1b, the initial coherent structure of a PbTe/GeTe nanocomposite consists of PbTe at the two ends with a lattice constant of 6.462 Å, and GeTe in the center with a lattice constant of 5.987 Å. Thirteen unit cells in the y and z dimensions are chosen for both components. This makes the y and z dimensions of the simulation box to be 84.002 Å. As for the x dimension, more than 100 Å for each component is sufficient to establish a temperature gradient and reveal the thermal transport parameters. Considering the interim portion adjacent to the interface, about 250 Å for the entire length in the x direction is chosen. Long-range Coulomb interaction should also be considered for these two ionic crystal materials. Thus, periodic boundary conditions are used in all three dimensions, and a particle–particle particle-mesh (PPPM) solver[47] is applied to calculate this long-range interaction instead of the traditional Ewald summation technique. This solver maps atom charge to a 3D mesh, uses 3D fast Fourier transformation (FFT) to solve Poisson's equation on the mesh, and then interpolates electric fields on the mesh points back to the individual atoms. The PPPM solver is a faster choice because its computation cost scales as $N \log(N)$ due to the FFTs, where N is the number of atoms in the system, while the cost of the traditional Ewald summation scales as $N^{3/2}$.[48] A Columbic cutoff can be specified, which means that pairwise interactions within this distance are computed directly and interactions outside that distance are computed in reciprocal space until the summation reaches the specified level of precision. For our simulation, the cutoff is given as 26 Å, and the precision of the summation is 10^{-4}. The dimensions of the structure from left to right exclude two interim portions are: $8.5a_{PbTe} \times 13a_{PbTe} \times 13a_{PbTe}$, $17.5a_{GeTe} \times 13a_{GeTe} \times 13a_{GeTe}$, and $8a_{PbTe} \times 13a_{PbTe} \times 13a_{PbTe}$. The velocity Verlet[49] algorithm is used for time integration of the motion equations of atoms. The initial structure is relaxed at 700 K for 100 ps to obtain equilibrium structure. Because of the possible large stress in the initial structure, a small time step $\Delta t = 0.1$ fs is used for 5 ps at the beginning to avoid atom blowing, which is then increased to 0.25 fs for the later computation. Isothermal–isobaric ensemble NPT is engaged at this equilibrium stage to reduce the stress in the system. Constant NPT integration is performed with Nosé/Hoover thermostat[50] and barostat.[51] After 5 ps with a 0.1 fs time step, another 100 ps computation is applied to reach equilibrium. It is believed that at this time the system is in equilibrium because the variation percentage of the potential energy in the last 5 ps is only about 2.6×10^{-6}. After equilibrium, the NEMD stage applying a heat flux of 5.4×10^9 W m^{-2} is engaged. A microcanonical ensemble NVE is used at this stage. 1500000 time steps (375 ps) is enough to obtain steady temperature profile after monitoring the fluctuation of statistical average temperature in each section.
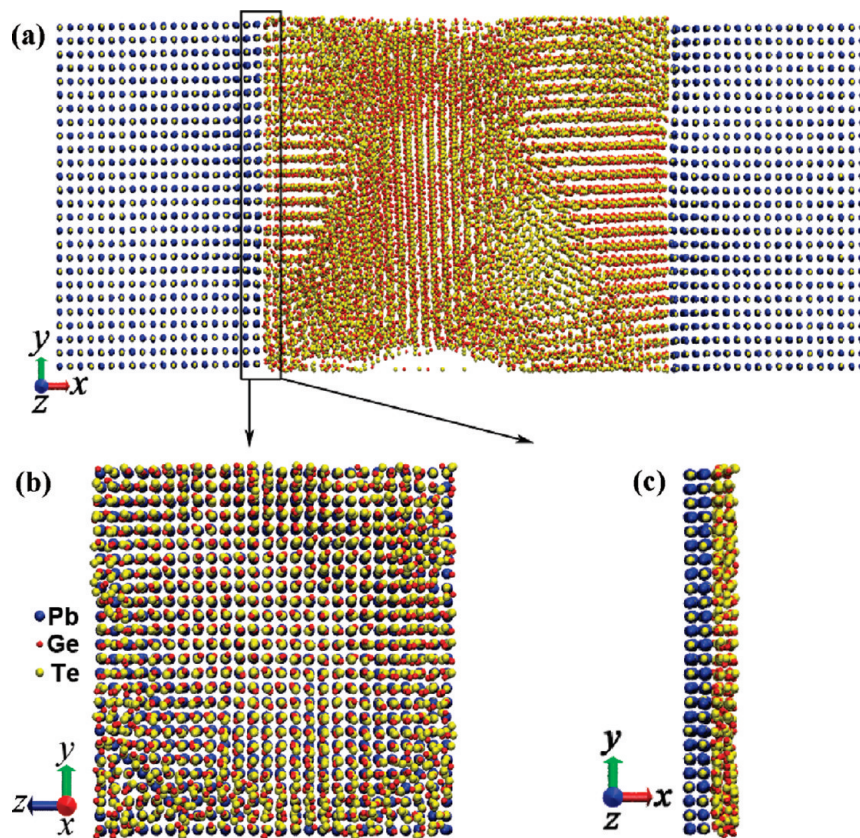
Figure 2. Observed equilibrium coherent structure near the PbTe/GeTe interface. (a) The entire structure; the left (negative *x*) interface viewed from (b) the positive *x* direction and (c) the positive *z* direction. Most area is incoherent except the four corners. The coherency of the structure across the interface can be observed by the atomic position overlap in part b.

3. Results and Discussions

3.1. Structure of Coherent Interface. The equilibrium structure visualized by a graphic program visual molecular dynamics (VMD)[52] is shown in Figure 2. Figure 2a corresponds to the entire system, and parts b and c of Figure 2 represent four atomic layers adjacent to the left interface viewed from the positive *x* direction and the positive *z* direction, respectively. It can be seen that the PbTe layers next to the interface retain perfect crystal structure, which means the initial reduced lattice constant is recovered by the strong and stable long-range Columbic interaction in PbTe. At the same time, the GeTe atomic planes are stretched to match the normal lattice of PbTe, which is observed within the first 10 ps trajectory of the system. As a result, the interface is seen to exhibit coherency although there is some disorder at the four corners of GeTe side. The coherency can be clearly viewed by the overlapped atomic positions in Figure 2b. The minor disorder observed in Figure 2b is due to the initial strain at the interface with periodic boundary conditions. In the central part of GeTe, disorder and dislocations are also observed as shown in Figure 2a, which could contribute to the reduced the thermal conductivity discussed later. The main reason for the disorder and dislocations in the GeTe is that the given temperature 700 K is near its phase transition temperature. PbTe has a high melting temperature of 1197 K, and there is no phase transition below this temperature. Therefore, GeTe rocksalt crystal structure at 700 K is not as stable as PbTe.

Figure 3 shows the equilibrium radial distribution functions (RDF) of different pairs in different regions of the structure. For PbTe, regardless of position within the structure, the locations of the peaks agree with those corresponding to a FCC crystal, as shown in Figure 3a. The lattice constant of PbTe at
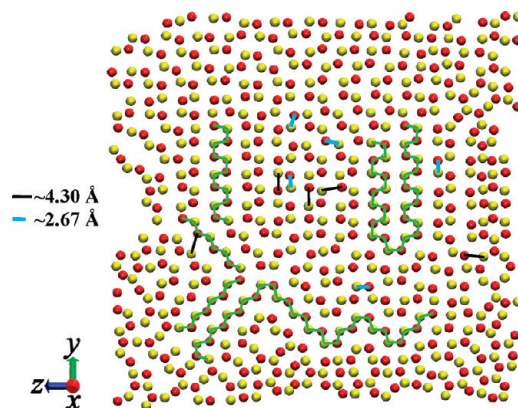
this state is calculated as 6.54 Å, which is about 1% larger than the initial lattice constant at 300 K. The possible reason could be its higher temperature or the proximity of the GeTe. For GeTe, the first peaks of Ge−Ge and Te−Te pairs are located at about 4.30 Å, which is close to the first peak of crystal at $0.707a_{GeTe}$. As for Ge−Te pairs, however, two peaks which do not exist in the RDF of GeTe crystal are seen; one at about 2.67 Å, and the other at about 4.30 Å. There should be only one peak about $0.5a_{GeTe}$, corresponding to 2.998 Å, in this range for Ge−Te pairs in the RDF of crystalline GeTe. The possible reason is that the FCC lattice is twisted, which results in both expansion and contraction of the Ge−Te atomic distances. The visualization of the first GeTe atomic layer adjacent to the left interface demonstrates this point, as shown in Figure 4. It is clearly seen that there are two lattice patterns in GeTe, trapezoid and zigzag, as sketched out by continuous solid lines. The three short edges in a trapezoid pattern and the edges in a zigzag pattern have the same average length at about 2.67 Å. The long edge in a trapezoid pattern and the Ge−Te distance in parallel zigzag patterns have the same average length of 4.30 Å. Obviously, the first length is dominant, which results in a much higher first peak than the second peak in the RDF distribution. It is conclusive that the initial GeTe crystal becomes twisted in order to match the PbTe lattice structure and to form a coherent interface.

3.2. Coherency of the Interface. To study the coherent interface structure quantitatively, the atom number density at the PbTe and GeTe side is studied. The atom number density *n* is defined as the number of atoms per unit volume within a specified region. Its distribution along a certain direction is a good way to reflect the crystallinity and coherency of a multicomponent structure. A simple moving window average

Coherent Nanointerfaces

J. Phys. Chem. C, Vol. 114, No. 49, 2010 **21007**
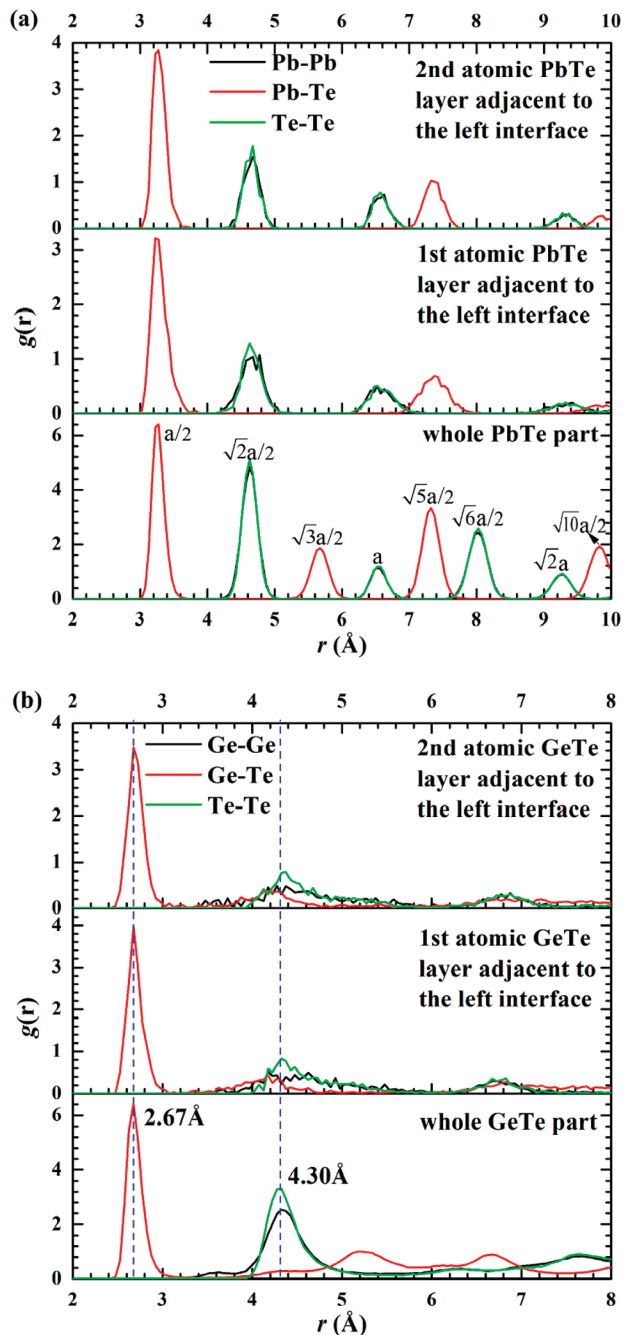
Figure 3. RDF of different pairs in the equilibrium coherent structure. (a) PbTe portion, $a = 6.54$ Å, in good FCC crystalline structure; (b) GeTe portion, the initial FCC lattice is twisted.

Figure 4. The *y-z* view of the first atomic GeTe layer adjacent to the interface. The FCC structure is twisted, and trapezoid and zigzag lattice patterns are observed. This agrees with the two peaks in previous RDF distribution. The solid black and blue lines in the figure are to illustrate the long and short bond lengths after lattice twisting.
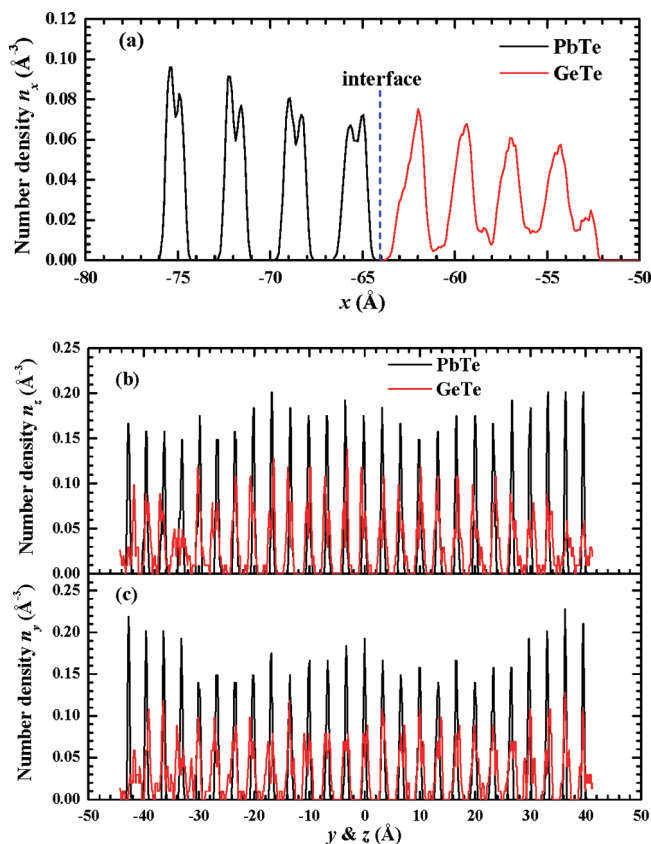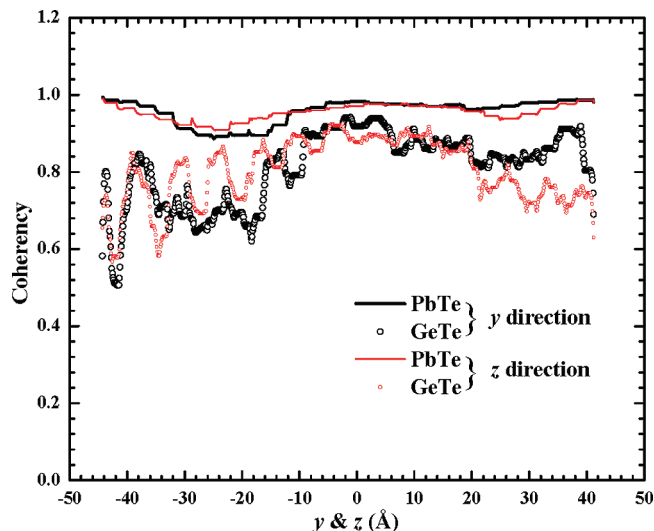

Figure 5. The atom number density distribution of PbTe and GeTe along the (a) *x*, (b) *y*, and (c) *z* directions. The PbTe is in good crystalline structure. Near PbTe peaks, there are always two GeTe peaks, which is due to two lattice patterns after the FCC lattice is twisted in GeTe.

method is used to calculate *n* in this work. The moving step is $a_{PbTe}/64$ (~ 0.1 Å), and the window size is $a_{PbTe}/16$. Figure 5 shows the atom number density distribution along the three directions in a specific region for the two components. To emphasize the interface and exclude the effect of the dislocation in the central GeTe region on the number density along the *y* and *z* directions, the region for *n* in the *x* direction is confined to four atomic layers next to the interface. The number density distribution in the *x* direction is shown in Figure 5a. Symmetrical and equispaced peaks for PbTe illustrate that the PbTe side exists in good crystalline order. Asymmetrical peaks and the absence of zero zones between peaks for GeTe indicate the GeTe side exhibits some disorder. The number density distribution along the *y* and *z* directions for the two components as shown in parts b and c of Figure 5 gives a rough idea of the coherency at the

interface. Extensive peak overlap is observed for the atom number density distribution in the *y* and *z* directions, indicating atomic coherency across the PbTe/GeTe interface.

To quantitatively describe the extent to which the atomic registry at the interface exhibits coherency, a coherency function based on the atom number density distribution is proposed,

$$\Phi_Y(y) = \frac{1}{\sum n_i} \sum n_i \left| \cos\left(\frac{y_i - Y_{peak}}{Y_{interval}} \pi \right) \right| \qquad (2)$$

Figure 6. The line coherency along the y and z directions for PbTe and GeTe. Solid line is for PbTe; open circle is for GeTe. Black, y direction; red, z direction.

where Y_{peak} is the coordinate of one peak in the atomic number density distribution along the y direction, $Y_{interval}$ the average peak−peak distance, and n_i the number density at y_i position. For the coherency calculation at location y, the number density within a range of $[y - Y_{interval}/4, y - Y_{interval}/4]$ is considered. The cosine term acts as a weight factor for the number density. If all atoms are perfectly located at the peak position, the coherency function will be 1. The subscript Y indicates that the coherency is for the y direction, and replacing the y variables with corresponding z variables in eq 2 can give the coherency along the z direction: $\Phi_Z(z)$. The main idea of this function is that an ideal n distribution of a crystal with Y_{peak} and $Y_{interval}$ is chosen for reference, and then deviations from perfect coherency are represented by departures of the evaluated n distribution from the ideal one. A coherency of 0 corresponds to an incoherent interface, while a coherency of 1 means perfect atomic registry. As shown in Figures 2a and 3a, the PbTe has good crystallinity, so its Y_{peak} and $Y_{interval}$ are used as the reference for the coherency study to determine the extent to which the GeTe structure follows that of PbTe. On the basis of Figure 3b, $Y_{peak} = 0$ and $Z_{peak} = 0$ are chosen, and the average peak distances are calculated as $Y_{interval} = 3.292$ Å and $Z_{interval} = 3.296$ Å. The coherency of the PbTe/GeTe interface defined by eq 2 along the y and z directions is plotted in Figure 6. For the PbTe, the coherency is almost 1 everywhere along the y and z directions, indicating that the PbTe retains its well-ordered crystalline structure near the interface. For GeTe, the coherency in areas close to its outside boundaries is imperfect but still larger than 0.5. Inside GeTe, its coherency is above 0.9, indicating that it retains a crystalline structure similar to that of PbTe (e.g., atomic distance) and also that the atom distribution in space agrees with that of PbTe.

The above-designed coherency Φ is one-dimensional. It reflects the structure consistence between two grouped lines and is termed line coherency. Figure 2a shows that some atoms in the two layers are nearly superpositioned (in the y and z directions), and some are dislocated. A 2D map of coherency is developed in order to quantitatively describe the coherency for each atom or a small area. Another function is proposed for this purpose, given by

$$\Psi_Y(y,z) = \frac{1}{N} \sum_{i=1}^{N} \left| \cos\left(\frac{y_i - Y_{peak}}{Y_{interval}} \pi \right) \right| \quad (3)$$

in which Y_{peak} and $Y_{interval}$ are the same as described previously. The simple moving window average method is also used. In eq 3, N is the total number of the atoms in a square area, y_i is the y coordinate of each atom in this area, and y and z are the coordinates of the center of this area. The moving steps along two directions are both $a_{PbTe}/64$, and the size of the 2D area is $Y_{interval} \times Z_{interval}$. The subscript Y in the function Ψ indicates that the coherency is for the y direction, and replacing the y variables with corresponding z variables gives the coherency $\Psi_Z(y,z)$ along the z direction. Every (y, z) point will have a coherency value, and this function is termed point coherency. To couple the deviation effect of two directions into the point coherency, we multiply the coherency along the two directions and obtain the square root of the product. Finally we have, $\Psi_{YZ}(y,z) = (\Psi_Y \Psi_Z)^{1/2}$.

Figure 7 shows the 2D map of point coherency $\Psi_Y(y,z)$, $\Psi_Z(y,z)$, and $\Psi_{YZ}(y,z)$ of PbTe and GeTe for the regions illustrated in Figure 2b. PbTe exhibits very good coherency as expected. Most of the area has a coherency value exceeding 0.95. For GeTe, the y end contains numerous dislocation along the y direction, and the two ends in the z direction also have many dislocations along the z direction. Even after combining the effects of the two directions, most areas of PbTe still retain coherency over 0.8 as shown in Figure 7e.

From the above discussions on line and point coherency, it is reasonable to conclude that the coherent nanointerface formed in PbTe/GeTe nanocomposites is favorable for electrical conduction while introducing high thermal resistance due to strong interface phonon scattering. This result provides guidance for developing an optimal degree of coherency for high ZT thermoelectric materials, giving the highest ratio of electrical to thermal conductivity.

3.3. Nanoscale Localized Strain. A high degree of local lattice strain at the interface has been observed in previous experimental work.[14] In this work, to form a coherent interface at the PbTe/GeTe nanocomposite, the lattice constant (atomic distance) of both materials must adjust to match each other at the interface. This causes localized strain near the interface. The adjustment of one component can be viewed as a result of the different atomic interaction from the other. The nearest neighboring distance (NND) is a parameter reflecting how close the atoms are to each other in a region. Comparing NND in different regions can reveal the relative strain. The system is partitioned into several sections along the x direction, as with the temperature profile calculation, and the resulting NND distribution is shown in Figure 8. It is clearly seen from the figure that the GeTe near the interface is expanded in the y-z plane by the PbTe. Actually, this is due to the repulsive force normal to y-z plane from PbTe rather than an attractive force in the y-z plane. The explanation is as follows. As detailed in previous discussions, the PbTe remains in nearly perfect crystalline order. For an FCC crystal, the value of NND should be half of the lattice constant. However, the calculated NND in most of the PbTe is 3.275 Å, which is larger than $0.5a_{PbTe}$ at 3.231 Å due to the expansion. NND in GeTe is smaller than $0.5a_{GeTe}$ as 2.998 Å due to the twisted lattice structure detailed above. The varying NND in GeTe indicates that regions near the interface have the largest strain while the central regions also exhibit some strain. The extent of such strain is within about 5−6 nm adjacent to the interface. The highest strain occurs at the interface, with a value of about 0.007. This can be thought of as pressed from

Coherent Nanointerfaces
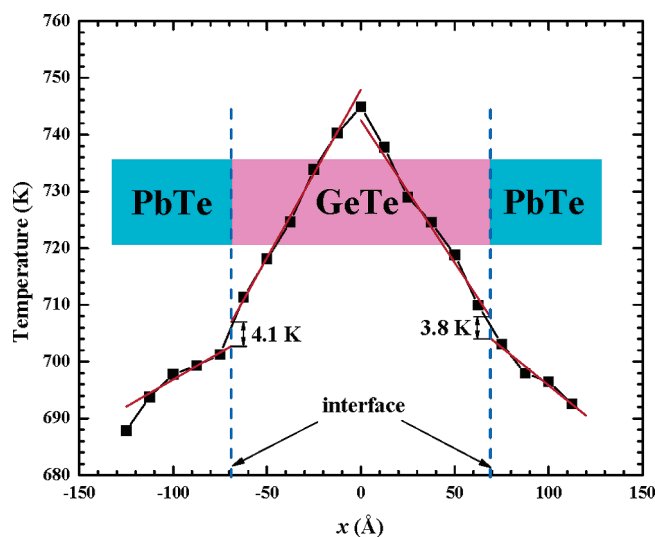
J. Phys. Chem. C, Vol. 114, No. 49, 2010 **21009**
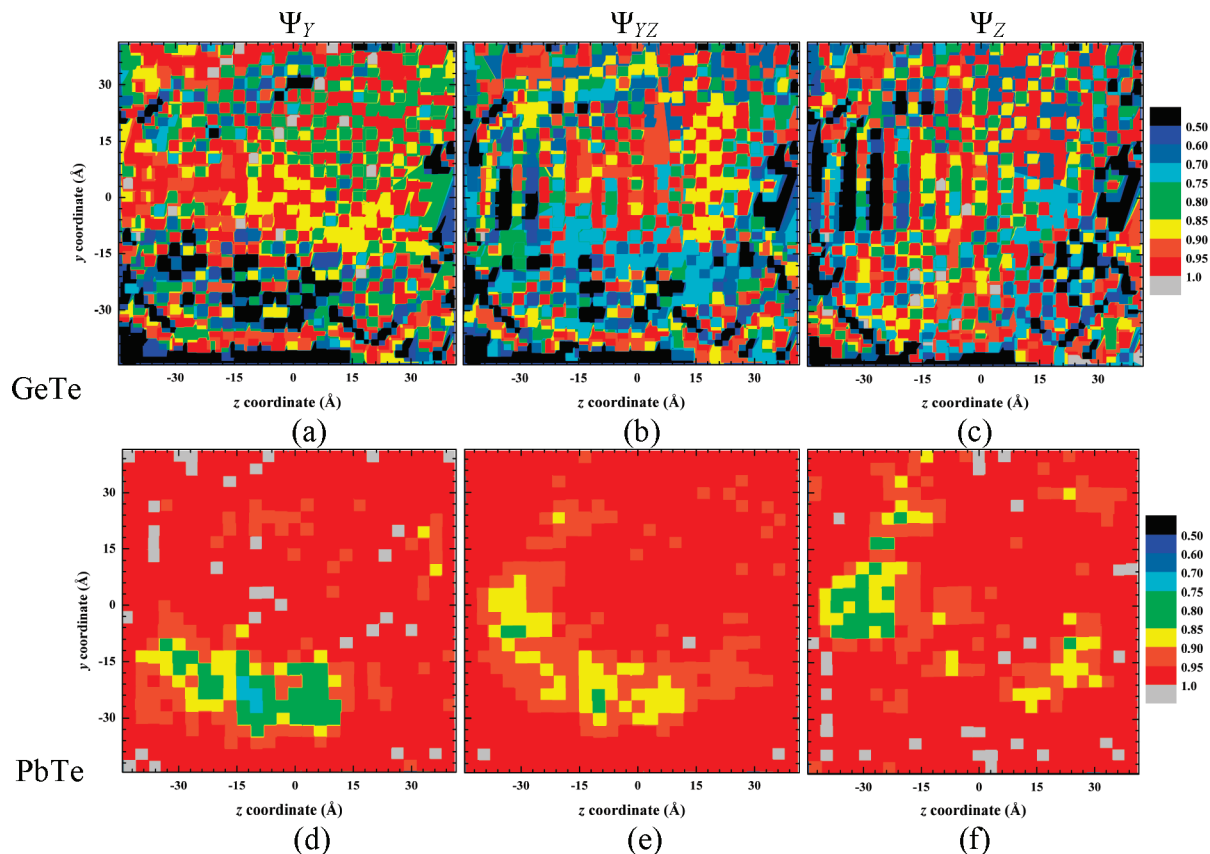
Figure 7. 2D map of point coherency of PbTe and GeTe in areas adjacent to the PbTe/GeTe interface. The calculation is for the regions illustrated in Figure 2b.
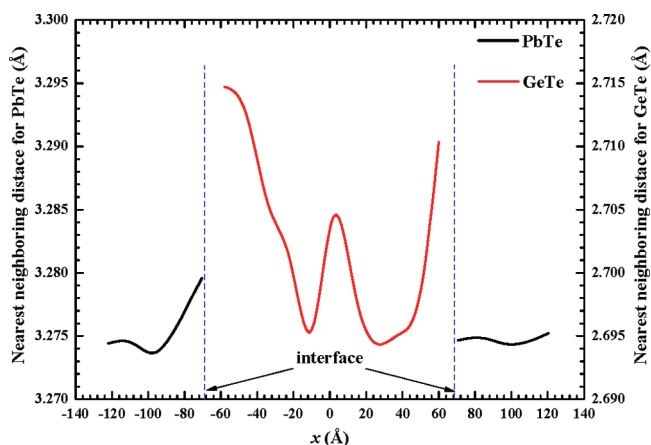
Figure 8. Distribution of the nearest neighboring distance for PbTe and GeTe along the x direction. It is shown that in GeTe the highest strain (tensile) of ~0.007 happens at the interface. The strain level in PbTe is much weaker (~0.001).

Figure 9. The temperature profile along the x direction of the structure at the equilibrium 700 K temperature. The least-squares linear fitting curve is also plotted. The vertical dash lines indicate the locations of the interfaces.

two sides by PbTe, and the GeTe near the interface responds by extending in the y and z directions. An extended region also exists in the center which is typical in the deformation of materials. Additionally, periodic slow up−down NND distribution will cause k_{lat} reduction while affecting electrical conductivity relatively little. The strong nanoscale localized strain especially in GeTe part will also enhance the phonon scattering and thus reduce lattice thermal conductivity.

3.4. Local Phonon Energy Thermal Transport. Figure 9 shows the temperature profile along the x direction at the equilibrium 700 K temperature. The heat flux applied after equilibrium is 5.4×10^9 W m^{-2} for 375 ps. The least-squares linear fittings at different portions that are used to obtain

temperature gradient and determine temperature drop across the interface are also shown. The standard deviation of fitting curves is used for estimation of uncertainty, applying the law of uncertainty propagation to the function $k(a_1, a_2)$ in which a_1 and a_2 are the slopes of the fitting curves for one component at two sides, respectively. The temperature that represents the hot and cold slabs is not used in the fitting because adding and removing energy makes them difficult to reach local thermal equilibrium (LTE). Therefore, from the fitted curves, the k_{lat} of PbTe and GeTe are 2.43 ± 0.39 W m^{-1} K^{-1} and 0.99 ± 0.07

TABLE 1: Lattice Thermal Conductivity of PbTe and GeTe at Different Temperatures from Experiments and MD Simulation ($W m^{-1} K^{-1}$)

|	PbTe		GeTe	
	300 K	700 K	300 K	700 K
experiment	crystal 2.0−3.5[39,57−59] nanostructure 1.3−2.5[23,24,53,58]	crystal 1.0[58] nanostructure 0.7−1.5[23,58,59]	crystal 4.2,[39,60] 3.5[61] amorphous 2.3[60]	crystal 1.3@500K,[60] 1.5[61] amorphous 2.5@500K[60]
MD simulation (this work)	crystal 3.89 ± 0.08	in nanocomposites 2.43 ± 0.39	no data	crystal with PBC 1.53 ± 0.05, with interspace, 1.78 ± 0.02; in nanocomposites 0.99 ± 0.07

$W m^{-1} K^{-1}$, respectively. The experimental k_{lat} of PbTe and GeTe are heavily affected by doping level and atomic ratio. Moreover, the quality of samples differs between various synthesis routes and processing treatments. Thus, there are no standard values of lattice thermal conductivity for these two materials. The experimental k_{lat} from several references and results from this work are listed in Table 1 for comparison purposes.

Normally, investigations on the thermoelectric properties of GeTe are based on GeTe alloys or composites; so relatively little data on nanoengineered pure GeTe is documented. Conversely, considerable research has been done on nanostructured PbTe, such as nanocomposites,[24] nanowire,[53] and superlattice,[23] the range of reported k_{lat} values at 300−700 K is 0.7−2.5 $W m^{-1} K^{-1}$. As shown in Table 1, our MD values of k_{lat} for PbTe in nanocomposites are higher than the experimental ones for both crystal and nanostructures. For GeTe, they are lower than the experimental ones for both crystal and amorphous. It should be mentioned that the reported lattice thermal conductivity of PbTe with 100−150 nm grains at 300 K by Martin et al. was over 2 $W m^{-1} K^{-1}$, which is higher than most other reported ones of PbTe nanostructures. However, it is still well below the one in this work which could be predicted at over 2.5 $W m^{-1} K^{-1}$ at 300 K if following the accepted trend in which the thermal conductivity of PbTe-based structure above room temperature decreases with the temperature.[58] This indicates that there could be some mechanisms contributing to the difference in the thermal conductivity of different PbTe nanostructures. Actually, the calculated values in this work cannot be treated as standard crystal nor noncrystal properties, because conditions in our designed nanocomposites and crystals/noncrystals are very different including defects and strain. Normally, there are always some impurities and defects in experimental samples, and the atomic ratios are not exactly stoichiometric. Additionally, most researchers studying PbTe deliberately use some particular processes such as high-pressure high-temperature (HPHT) and annealing methods in fabricating the samples to reduce the thermal conductivity. Therefore, it is not surprising that our calculated thermal conductivity in crystalline PbTe is higher than that reported for experimental crystals and nanostructures. To strengthen our argument, the pure crystalline PbTe and GeTe of the same size as the PbTe/GeTe structure in three dimensions with periodic boundary conditions (PBC) are also studied by MD simulation in this work. The structures retain their crystalline order as observed by VMD, and the temperature profile is smooth. The results shown in Table 1 illustrate the measured lattice thermal conductivity of PbTe is up to 49% lower than the one predicted by NEMD. As for GeTe, the internal strong strain and dislocations make it not as effective at conducting heat as the experimental crystal. The MD value of k_{lat} at 700 K of pure crystalline GeTe is 1.53 ± 0.05 $W m^{-1} K^{-1}$, very close to the experimental data as 1.5 $W m^{-1} K^{-1}$. Considering the impurities and defects in experimental samples, the MD prediction gives

a reasonable value. The possible reasons for the difference could be: (1) computation and measurement uncertainty; (2) the computation size effect to introduce a lower thermal conductivity; (3) the effectiveness of the potential and its parameters applied to GeTe.

The strain effect is revealed after comparing the pure crystalline GeTe case with the coherent case. The thermal conductivity is decreased by 35% due to the strain and dislocations. It should be pointed out that the initial coherent PbTe/GeTe structure leaves some interspace around GeTe with the periodic boundary conditions. This might make a difference for thermal transport properties. Another case considering the interspace on pure GeTe simulation is also investigated. The same size interspace is added into the y and z directions of the simulation box while keeping the structure in the x direction periodically connected. The result gives 1.78 ± 0.02 $W m^{-1} K^{-1}$, which is 15% higher than that without interspace. The RDF of Ge−Te pairs in these different cases are shown in Figure 10. The lower first peak of the RDF in the coherent structure and the flat tail peaks illustrate that there are numerous dislocations in the GeTe portion. The fluctuated strain is the major factor reducing k_{lat} of the GeTe portion. For the crystal with interspace, the position of the first peak is 2.87 Å, which is slightly smaller than in the no-interspace case. With the same crystal structure, smaller bond length should give higher thermal conductivity. This could be the reason why the crystalline GeTe with interspace has a slightly higher thermal conductivity.

The effective thermal conductivity is more important in practice for nanocomposites. With the assumption that the thermal conductivity is uniform in the same component, the fitting curves of temperature profiles are extended to the hot
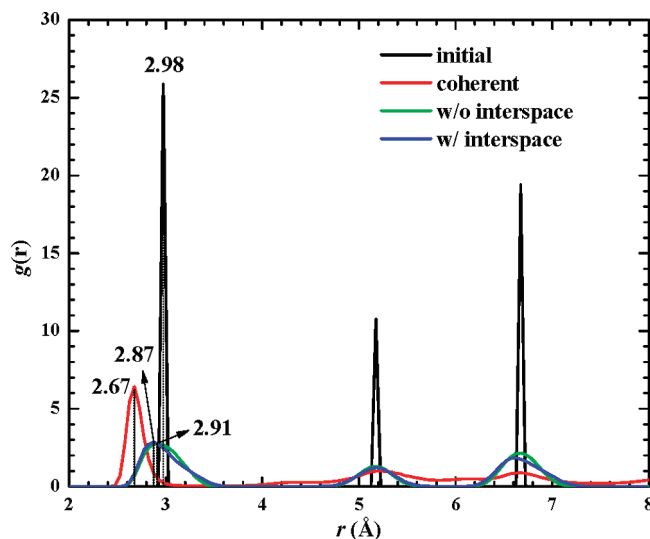

Figure 10. RDF of Ge−Te pairs at the equilibrium state in the coherent structure, pure GeTe crystal with and without interspace added into the y and z dimensions, and RDF of Ge−Te pairs at the initial state.

Coherent Nanointerfaces

J. Phys. Chem. C, Vol. 114, No. 49, 2010 **21011**

and cold slabs to obtain the real LTE temperature. Then the effective temperature gradient is calculated as the temperature difference between the hot and cold slabs divided by the distance between the hot and cold slabs. On the basis of Fourier's law, the effective k_{lat} of this structure is 1.23 ± 0.02 W m^{-1} K^{-1}. It is lower than the thermal conductivity of many common thermoelectric materials, which are not nanoengineered. The lower value is contributed by the strong localized strain and acoustic mismatch at the interface. Additionally, the structure distortion in the GeTe body (shown in Figure 2) reduces its thermal conductivity to a great extent. This also contributes to the overall thermal conductivity reduction of the nanocomposite. Compared with other specifically designed thermoelectric materials, such as melt quenched PbTe-Ge (10%) eutectic composites at 600 K (1.21 W m^{-1} K^{-1}) and PbTe-Ge (20%) doped with 0.037% PbI$_2$ at 650 K (1.25 W m^{-1} K^{-1}),[22] the value of this configuration is not so promising in terms of thermal conductivity reduction. On the other hand, the coherent interface structure is expected to have little effect on electrical conductivity, which is preferred for high-performance thermoelectric materials. On the basis of our MD results, the estimation on the effective thermal conductivity of bulk PbTe/GeTe composites with other sizes and volume fractions of compositions is feasible. In the past, a variety of methods have been proposed to estimate thermal properties of heterogeneous media including effective-medium approximation (EMA), Maxwell–Eucken approximation,[54] and Nan-Birringer approximation.[55] However, the first two do not take into account the interfacial thermal resistance, and the third one is for polycrystal of a single material. Hasselman and Johnson[56] proposed a predictive model considering the interfacial thermal resistance, which is appropriate for our system. It gives the effective lattice thermal conductivity of the bulk composite, k_{eff}, as

$$k_{eff} = k_2 \frac{\alpha + 2\beta}{\alpha - \beta} \quad (4)$$

where $\alpha = k_1/k_2 + 4k_1R''_{tc}/D + 2$, $\beta = f(k_1/k_2 - 2k_1R''_{tc}/D - 1)$, subscript 1 and 2 denote the inclusion and matrix phase, f the volume fraction of the inclusion, k the grain thermal conductivity, R''_{tc} the interfacial thermal resistance, and D the average grain size. From the temperature profiles in Figure 9, the temperature drops across the two interfaces are 4.1 and 3.8 K, respectively. R''_{tc} at the interface is calculated as $7.3 \pm 0.3 \times 10^{-10}$ m^2 K W^{-1}, which is slightly lower than the common observed values on the order of 10^{-9} m^2 K W^{-1} for interfaces. This is not surprising because a coherent interface results in less phonon scattering than at noncoherent interfaces. With the assumption that coherent interfaces are formed in the bulk PbTe/GeTe composites and have the same interfacial thermal resistance and by neglecting the size effect on the lattice thermal conductivity of the inclusion, the variation of the effective thermal conductivity k_{eff} with inclusion size at different volume fractions is predicted by the Hasselman–Johnson approximation as shown in Figure 11. GeTe is treated as the inclusion phase. Because of the low thermal conductivity of GeTe caused by dislocations and high degree of local strain, the k_{eff} decreases with the volume fraction of GeTe inclusion. The GeTe inclusion with the size smaller than 10 nm significantly decreases the k_{eff}. If the size effect on lattice thermal conductivity is considered, the predicted effective thermal conductivity for composites with a smaller grain size will obviously be lower than that shown in Figure 11, and the one for composites with a larger grain size will be higher. Because the competition of the attenuated effect
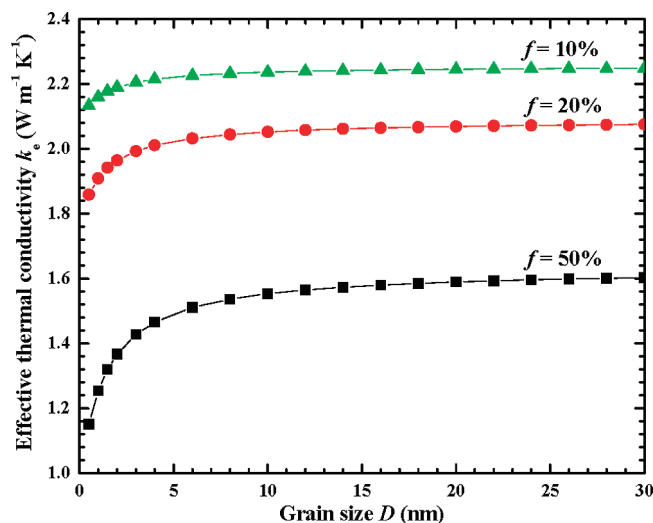
Figure 11. The effective thermal conductivity of PbTe/GeTe composites varies with the inclusion size at different volume fraction. GeTe is taken as the inclusion phase.

of interfacial coherency and the enhanced effect of the nanoscale localized strain adjacent to the interface on phonon scattering, the bulk k_{eff} value shown in Figure 11 is not very promising compared with some other nanostrutured materials. However, the potential to retain large electrical conductivity and to increase the thermal power makes PbTe/GeTe coherent structures a good candidate to achieve high *ZT*.

4. Conclusion

In this work, detailed MD simulation was carried out to explore the existence of coherent interfaces in PbTe/GeTe nanocomposites. This work was motivated by direct observation of coherent structures in the interface region. PbTe retained its original FCC structure while GeTe reconfigured itself by a twisting distortion to match the structure of PbTe at the interface. The atomic number density distribution clearly proved the existence of interfacial coherency. Line and point coherency functions showed that coherency existed in PbTe and GeTe adjacent to their interface. Nanoscale (5–6 nm) localized strain was observed in GeTe, with the highest strain of 0.007 at the interface. The existence of such localized strain gives rise to a phonon scattering mechanism at the interface. The effective lattice thermal conductivity of the PbTe/GeTe nanocomposite was calculated as 1.23 W m^{-1} K^{-1}, which is lower than the thermal conductivity of many common thermoelectric materials. The interfacial thermal resistance in this structure is $7.3 \pm 0.3 \times 10^{-10}$ m^2 K W^{-1}, which is slightly lower than the common observed values in the order of 10^{-9} m^2 K W^{-1} for interfaces. This could be due to less phonon scattering at the coherent interface. Future engineered nanocomposites with precisely designed interfaces offer a promising route to achieve increased *ZT* values.

References and Notes

(1) Hyun, D. B.; Hwang, J. S.; Shim, J. D.; Oh, T. S. *J. Mater. Sci.* **2001**, *36*, 1285.
(2) Culp, S. R.; Simonson, J. W.; Poon, S. J.; Ponnambalam, V.; Edwards, J.; Tritt, T. M. *Appl. Phys. Lett.* **2008**, *93*, 022105.

(3) Harman, T. C.; Taylor, P. J.; Walsh, M. P.; LaForge, B. E. *Science* **2002**, *297*, 2229.

(4) Wang, R. Y.; Feser, J. P.; Lee, J. S.; Talapin, D. V.; Segalman, R.; Majumdar, A. *Nano Lett.* **2008**, *8*, 2283.

(5) Sootsman, J. R.; Kong, H.; Uher, C.; D'Angelo, J. J.; Wu, C. I.; Hogan, T. P.; Caillat, T.; Kanatzidis, M. G. *Angew. Chem., Int. Ed.* **2008**, *47*, 8618.

(6) Wang, X. W.; Lee, H.; Lan, Y. C.; Zhu, G. H.; Joshi, G.; Wang, D. Z.; Yang, J.; Muto, A. J.; Tang, M. Y.; Klatsky, J.; Song, S.; Dresselhaus, M. S.; Chen, G.; Ren, Z. F. *Appl. Phys. Lett.* **2008**, *93*, 193121.

(7) Wu, Y. Y.; Fan, R.; Yang, P. D. *Nano Lett.* **2002**, *2*, 83.

(8) Hsu, K. F.; Fu, S. L.; Chen, G. W.; Dyck, J. S.; Uher, C.; Hogan, T.; Polychroniadis, E. K.; Kanatzidis, M. G. *Science* **2004**, *303*, 818.

(9) Quarez, E.; Hsu, K. F.; Pcionek, R.; Frangis, N.; Polychroniadis, E. K.; Kanatzidis, M. G. *J. Am. Chem. Soc.* **2005**, *127*, 9177.

(10) Androulakis, J.; Hsu, K. F.; Pcionek, R.; Kong, H.; Uher, C.; DAngelo, J. J.; Downey, A.; Hogan, T.; Kanatzidis, M. G. *Adv. Mater.* **2006**, *18*, 1170.

(11) Zhou, M.; Li, J. F.; Kita, T. *J. Am. Chem. Soc.* **2008**, *130*, 4527.

(12) Wang, H.; Li, J. F.; Nan, C. W.; Zhou, M.; Liu, W. S.; Zhang, B. P.; Kita, T. *Appl. Phys. Lett.* **2006**, *88*, 092104.

(13) Hogan, T. P.; Downey, A.; Short, J.; D'Angelo, J.; Wu, C. I.; Quarez, E.; Androulakis, J.; Poudeu, P. F. P.; Sootsman, J. R.; Chung, D. Y.; Kanatzidis, M. G.; Mahanti, S. D.; Timm, E. J.; Schock, H.; Ren, F.; Johnson, J.; Case, E. D. *J. Electron. Mater.* **2007**, *36*, 704.

(14) Cook, B. A.; Kramer, M. J.; Harringa, J. L.; Han, M. K.; Chung, D. Y.; Kanatzidis, M. G. *Adv. Funct. Mater.* **2009**, *19*, 1254.

(15) Gelbstein, Y.; Dashevsky, Z.; Dariel, M. P. *J. Appl. Phys.* **2008**, *104*, 033702.

(16) Martin, J.; Wang, L.; Chen, L.; Nolas, G. S. *Phys. Rev. B* **2009**, *79*, 115311.

(17) Yan, Q. Y.; Cheng, H.; Zhou, W. W.; Hng, H. H.; Boey, F. Y. C.; Ma, J. *Chem. Mater.* **2008**, *20*, 6298.

(18) Yang, Y. A.; Taggart, D. K.; Brown, M. A.; Xiang, C. X.; Kung, S. C.; Yang, F.; Hemminger, J. C.; Penner, R. M. *ACS Nano* **2009**, *3*, 4144.

(19) Hu, J. Q.; Chen, Z. G.; Jiang, H.; Sun, Y. G.; Bando, Y.; Golberg, D. *J. Mater. Chem.* **2009**, *19*, 3063.

(20) Zhu, T. J.; Yan, F.; Zhao, X. B.; Zhang, S. N.; Chen, Y.; Yang, S. H. *J. Phys. D* **2007**, *40*, 6094.

(21) Heremans, J. P.; Jovovic, V.; Toberer, E. S.; Saramat, A.; Kurosaki, K.; Charoenphakdee, A.; Yamanaka, S.; Snyder, G. J. *Science* **2008**, *321*, 554.

(22) Sootsman, J. R.; He, J. Q.; Dravid, V. P.; Li, C. P.; Uher, C.; Kanatzidis, M. G. *J. Appl. Phys.* **2009**, *105*, 083718.

(23) Koh, Y. K.; Vineis, C. J.; Calawa, S. D.; Walsh, M. P.; Cahill, D. G. *Appl. Phys. Lett.* **2009**, *94*, 153101.

(24) Martin, J.; Nolas, G. S.; Zhang, W.; Chen, L. *Appl. Phys. Lett.* **2007**, *90*, 222112.

(25) Ikeda, T.; Collins, L. A.; Ravi, V. A.; Gascoin, F. S.; Haile, S. M.; Snyder, G. J. *Chem. Mater.* **2007**, *19*, 763.

(26) Chou, F.-C.; Lukes, J. R.; Liang, X.-G.; Takahashi, K.; Tien, C.-L. *Annu. Rev. Heat Trans.* **1999**, *10*, 141.

(27) Chen, G.; Tasciuc, Borca; Yang, R. In *Encyclopedia of Nanoscience and Nanotechnology*, Nalwa, H. S., Ed.; American Scientific Publishers: Stevenson Ranch, CA, 2004; Vol. 7, p 429.

(28) Maiti, A.; Mahan, G. D.; Pantelides, S. T. *Solid State Commun.* **1997**, *102*, 517.

(29) Maruyama, S.; Kimura, T. *Therm. Sci. Eng.* **1999**, *7*, 63.

(30) Stevens, R. J.; Zhigilei, L. V.; Norris, P. M. *Int. J. Heat Mass Trans.* **2007**, *50*, 3977.

(31) Zhong, H. L.; Lukes, J. R. *Phys. Rev. B* **2006**, *74*, 125403.

(32) Kaddouri, H.; Benet, S.; Charar, S.; Makowaska-Janusik, M.; Tedenac, J. C.; Kityk, I. V. *Phys. Rev. B* **2000**, *62*, 17108.

(33) Chonan, T.; Katayama, S. *J. Phys. Soc. Jpn.* **2006**, *75*, 064601.

(34) Lee, J. H.; Galli, G. A.; Grossman, J. C. *Nano Lett.* **2008**, *8*, 3750.

(35) Huang, X. P.; Huai, X. L.; Liang, S. Q.; Wang, X. W. *J. Phys. D* **2009**, *42*, 095416.

(36) Landry, E. S.; McGaughey, A. J. H. *Proceedings of the ASME Summer Heat Transfer Conference* **2009**, *Vol 1*, 413. *HT2008*.

(37) Chattopadhyay, T.; Boucherle, J. X.; Vonschnering, H. G. *J. Phys. C* **1987**, *20*, 1431.

(38) Rabe, K. M.; Joannopoulos, J. D. *Phys. Rev. B* **1987**, *36*, 6631.

(39) Clasen, R.; Grosse, P.; Krost, A.; Levy, F.; Marenkin, S. F.; Richter, W.; Ringelstein, N.; Schmechel, R.; Weiser, G.; Werheit, H.; Yao, M.; Zdanowicz, W. *Non-Tetrahedrally Bonded Elements and Binary Compounds I*; Springer: New York, 1998.

(40) De Bellis, L.; Phelan, P. E.; Prasher, R. S. *J. Thermophys. Heat Trans.* **2000**, *14*, 144.

(41) Prasher, R. S.; Phelan, P. E. *J. Heat Trans.* **2001**, *123*, 105.

(42) Beechem, T.; Graham, S.; Hopkins, P.; Norris, P. *Appl. Phys. Lett.* **2007**, *90*, 054104.

(43) Duda, J. C.; Smoyer, J. L.; Norris, P. M.; Hopkins, P. E. *Appl. Phys. Lett.* **2009**, *95*, 031912.

(44) Ikeshoji, T.; Hafskjold, B. *Mol. Phys.* **1994**, *81*, 251.

(45) Slack, G. A. In *CRC Handbook of Thermoelectrics*; Rowe, D. M., Ed.; CRC Press: Boca Raton, USA, 1995; p 407.

(46) Finegold, L. *Phys. Rev. Lett.* **1964**, *13*, 233.

(47) Hockney, R. W.; Eastwood, J. W. *Computer Simulation Using Particles*; Taylor & Francis Group: New York, 1988.

(48) Pollock, E. L.; Glosli, J. *Comput. Phys. Commun.* **1996**, *95*, 93.

(49) Swope, W. C.; Andersen, H. C.; Berens, P. H.; Wilson, K. R. *J. Chem. Phys.* **1982**, *76*, 637.

(50) Nosé, S. *J. Chem. Phys.* **1984**, *81*, 511.

(51) Hoover, W. G. *Phys. Rev. A* **1986**, *34*, 2499.

(52) Humphrey, W.; Dalke, A.; Schulten, K. *J. Mol. Graph.* **1996**, *14*, 33.

(53) Roh, J. W.; Jang, S. Y.; Kang, J.; Lee, S.; Noh, J. S.; Kim, W.; Park, J.; Lee, W. *Appl. Phys. Lett.* **2010**, *96*, 103101.

(54) Wang, J.; Carson, J. K.; North, M. F.; Cleland, D. J. *Int. J. Heat Mass Trans.* **2008**, *51*, 2389.

(55) Nan, C.-W.; Birringer, R. *Phys. Rev. B* **1998**, *57*, 8264.

(56) Hasselman, D. P. H.; Johnson, L. F. *J. Compos. Mater.* **1987**, *21*, 508.

(57) Kishimoto, K.; Koyanagi, T. *J. Appl. Phys.* **2002**, *92*, 2544.

(58) Sootsman, J. R.; Pcionek, R. J.; Kong, H.; Uher, C.; Kanatzidis, M. G. *Chem. Mater.* **2006**, *18*, 4993.

(59) McGuire, M. A.; Malik, A. S.; DiSalvo, F. J. *J. Alloys Compd.* **2008**, *460*, 8.

(60) Nath, P.; Chopra, K. L. *Phys. Rev. B* **1974**, *10*, 3412.

(61) Bursian, E. V.; Kalimullin, R. K. *Ferroelectr.* **1995**, *168*, 91.